Beam dynamics studies for fast beam trip recovery of the Japan Atomic Energy Agency accelerator-driven subcritical system

Bruce Yee-Rendon,* Yasuhiro Kondo, Jun Tamura, Keita Nakano, Fujio Maekawa, and Shin-ichiro Meigo

Japan Proton Accelerator Research Complex (J-PARC) Center, Japan Atomic Energy Agency, Tokai, Ibaraki 319-1195, Japan

(Received 22 April 2022; accepted 12 July 2022; published 5 August 2022)

High reliability and availability are primary goals for the operation of particle accelerators, especially for accelerator-driven subcritical systems (ADS). ADSs employ high-power beams for the transmutation of minor actinide; as a result, the amount and the radiotoxicity of the nuclear waste are considerably reduced. To this end, the Japan Atomic Energy Agency is designing a 30-MW continuous wave (cw) superconducting proton linear accelerator (linac) that supplies neutrons to an 800-MW subcritical reactor by a spallation process. The major challenge for an ADS linac is the strict control of the beam trip duration and its frequency to avoid thermal stress in the subcritical reactor structures. The maximum allowed beam trips for failures longer than a few seconds are estimated to be far below the rate achieved in current accelerators. Thus, we implemented a combination of hot standby and local compensation that enables a fast beam recovery. This work comprehensively investigated the tolerance of our linac lattice for the local compensations for failures in superconducting cavities and magnets. This scheme includes simultaneous compensation of multiple cavities in independent and same cryomodules that significantly enhance the reliability of the linac. The retuned schemes present acceptable beam performance to guarantee the integrity of the linac and the beam transport to the target; moreover, they satisfy the beam stability in the beam window. In addition, the readjusted elements are subjected to moderate stress to ensure a sustainable operation. This manuscript reports the beam dynamics results toward fulfilling the high reliability demanded by an ADS linac.

DOI: 10.1103/PhysRevAccelBeams.25.080101

I. INTRODUCTION

The Japan Atomic Energy Agency (JAEA) is developing an accelerator-driven subcritical system (ADS) to reduce the geological burden of nuclear waste by transmuting minor actinides. The JAEA-ADS uses a 30-MW continuous wave (cw) superconducting proton linear accelerator (linac) to produce neutrons by a spallation process with a lead-bismuth eutectic (LBE) target for an 800-MW thermal power subcritical reactor [1]. Figure 1 shows the conceptual design of the JAEA-ADS project.

A crucial feature of the ADS accelerator is the stringent reliability to avoid thermal stress in the subcritical reactor structures, which is beyond the reach of the current high-intensity machines [2]. Thus, the ADS accelerator pursues a reliability-oriented accelerator to satisfy that requirement [3–6].

Table I presents the most relevant parameters of the JAEA-ADS linac, which is composed of a normal conducting part and a superconducting one [7]. The superconducting section, known as the main linac, accelerates a 20 mA proton beam from 2.5 MeV to 1.5 GeV by using three different superconducting radio frequency (SRF) cavities operating at different frequencies: half-wave resonator (HWR) operates at 162 MHz, single-spoke resonator (SSR), at 324 MHz, and five-cell elliptical resonator (EllipR), at 648 MHz. The last two types of SRF cavities, SSR and EllipR, have two families for a high beam accelerating efficiency. Table II provides detail of the main linac configuration. The main linac lattice was optimized to have a robust design with a simple period configuration, strict control of beam loss, and operates with derated SRF cavities to reduce the probability of failure by keeping the electric field peak on the cavity's surface up to 30 MV/m. In addition, the accelerating gradient (E_{acc}) and the synchronous phase (ϕ_s) of the SRF cavities were tuned to preserve the longitudinal phase acceptance, as shown in Fig. 2. Moreover, each SRF cavity is associated with a

*byee@post.j-parc.jp

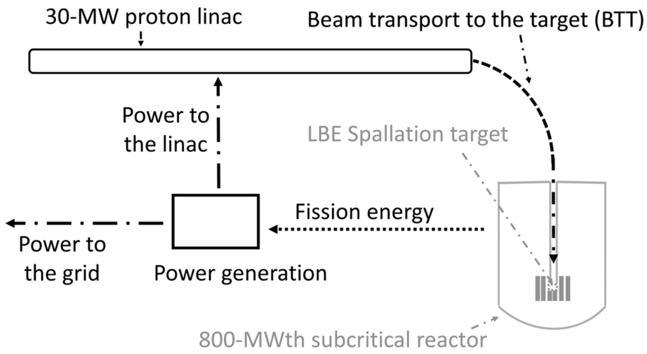

FIG. 1. General scheme for the JAEA-ADS.

single rf source for independent control. The derated operation, which allows a retuned margin of 20% in the E_{acc}, wide longitudinal acceptance, and one-to-one rf source—SRF cavity configuration enhances the linac capability to compensate for an SRF cavity failure [8–10].

After achieving a robust linac that operates with low E_{acc} values to reduce the probability of SRF cavity trips, we implemented tolerance studies for the fault compensation operation to accomplish a quick beam resumption after the failure in linac elements by using redundancy schemes. High fault tolerance is pursued by applying a combination of hot standby and local compensation schemes [3]. The hot standby scheme consists of a duplication structure, with one system as the major operator and the other as offline-powered equipment ready to operate in case of a failure in the principal structure. The local compensation is based on *k-out-of-n* redundancy configuration, which states that a system composed of *n* elements needs at least *k* of its components to operate [3,11,12]. With this compensation scheme, fast linac recovery can be achieved, but the beam performance of the compensated lattice must be acceptable.

TABLE I. Main characteristics of the JAEA-ADS accelerator [7].

Parameter		Beam trip duration
Particle	Proton	
Beam current (mA)	20	
Beam energy (GeV)	1.5	
Duty factor (%)	100 (cw)	
Beam loss[a] (W/m)	< 0.02	
$\varepsilon_{\mathrm{norm,rms},x}$[b] ($\pi$ mm mrad)	0.20/0.26	
$\varepsilon_{\mathrm{norm,rms},y}$[b] ($\pi$ mm mrad)	0.21/0.29	
$\varepsilon_{\mathrm{norm,rms},z}$[b] ($\pi$ MeV deg)	0.07/0.08	
Operating time per year (h)	7200	
Beam trips per year [2]	2×10^4	≤ 10 s
	2×10^3	From 10 s to 5 min
	42	> 5 min
Length (m)	429	

[a]At the entrance of the first half-wave resonator (HWR) cryomodule obtained from beam tracking simulations [7].
[b]At the main linac entrance/end obtained from beam tracking simulations [7].

TABLE II. Main linac parameters and configurations.

Parameter	HWR	SSR1	SSR2	EllipR1	EllipR2
Final energy (MeV)	17.7	49.4	208.8	583.4	1500
Frequency (MHz)	162	324	324	648	648
Number of cavities	25	66	72	60	70
Maximum E_{acc} (MV/m)	7.1	6.6	8.5	13.8	14.2
Layout[a]	S-C	S-C^2	S-C^3	DQ-C^3	DQ-C^5
Number of periods	25	33	24	20	14
Number of cryomodules per period	9-8-8[b]	1	1	1	1
Cryomodules length[c] (m)	0.7	1.7	3.4	5.7	9.9

[a]S stands for the superconducting solenoid, C is for the SRF cavity, and DQ is for the normal doublet quadrupole. The exponent over the C refers to the number of times the element appears in the lattice, i.e., C^m means that m SRF cavities have that period.
[b]The HWR section contains three cryomodules: the first one with nine periods and the other two with eight.
[c]Solenoids are inside the cryomodules, but quadrupoles are not.

In this paper, the tolerance of the JAEA-ADS lattice for the fault compensation operation is comprehensively surveyed.

Typical ADS fault tolerance studies were focused on compensations of single SRF cavities and magnets in the whole linac [13,14]. Compensation schemes have been improved to handle multiple Faulty elements simultaneously throughout the linac [10,15–17]. The reliability of the linac is boosted by increasing the number of cavities or magnets that can be compensated at the same time. For a system that

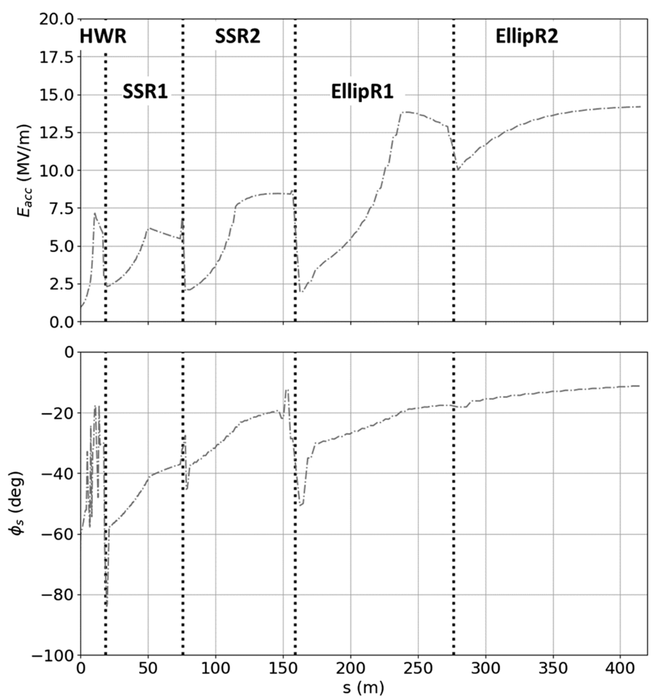

FIG. 2. Accelerating gradient (top) and synchronous phase (bottom) of the SRF cavities. The vertical lines show the transition between different SRF sections.

comprises many identical elements, such as linacs, compensation of one component is the basic application of *k-out-of-n* redundancy. However, the reliability is higher than the series configuration. Please see Sec. II for more details.

This study performed an extensive analysis that started with individual SRF cavity failures and extended to multiple SRF cavities that compose whole individual lattice periods, up to five SRF cavities for the last section, to improve accelerator reliability. In addition, it included single solenoids and doublet quadrupole compensations. Moreover, the retuned schemes satisfied rigorous constraints based on the linac, beam transport to the target (BTT), and the beam window requirements. The BTT has the important function of broadening the beam profile on the target to control the heat load density in the beam window. The change in the beam parameter at the input of the BTT may significantly affect the beam delivered to the beam window; thus, it could increase the thermal stress at the beam window, compromising the ADS operation.

Section II describes the redundancies strategies and the local compensation implementation. Then, the beam dynamics results are reported in Sec. III. Finally, Sec. IV provides the conclusions of this study.

II. REDUNDANCY STRATEGIES

As mentioned in the Introduction, we are planning to adopt a hybrid scheme that uses a hot standby injector from the beam source until some of the first SRF sections and local compensation for the rest of the linac. This strategy is adopted because, at low energies, the hot standby approach is more effective than local compensations. Moreover, if the low-energy beam elements are chosen to apply the hot standby strategy, the number of elements to duplicate is decreased, giving lower construction and maintenance costs.

The reliability of a system using a *k-out-of-n* configuration with identical modules is [3,11,12]

$$R_{\mathrm{Tot}} = \sum_{i=k}^{n} \frac{n!}{i!(n-i)!} R^{i}(1-R)^{n-i}, \tag{1}$$

where R is the reliability of one module, e.g., it is the probability that the module will be able to perform as demanded under given working conditions for a specified interval of time.

For a system with a series configuration with n modules, the reliability is given by

$$R_{\mathrm{Tot}} = \prod_{i=1}^{n} R_i, \tag{2}$$

where R_i is the reliability of the i module. Series configuration is considered a special case of *k-out-of-n* configuration when identical modules are assumed. For the case that all the elements are required to operate, which is the definition of a series configuration, Eq. (1) becomes R^n. Nevertheless, R^n is the same result as Eq. (2) for $R_i = R$. Now, if the linac can continue operating with only $n-1$ modules, the reliability becomes $R^n + nR^{n-1}(1-R)$ by using Eq. (1). Thus, the linac reliability is boosted by increasing the elements that can be compensated simultaneously.

For repairable systems, availability is commonly used instead of reliability as a figure of merit [3,11]. Availability is the probability that a system is properly operating when it is required, and it has the following simple steady-state representation:

$$\begin{aligned} A &= \frac{\text{System uptime}}{\text{Total time}}, \\ &= \frac{\text{System uptime}}{\text{System uptime} + \text{System downtime}}, \end{aligned} \tag{3}$$

where Total time is the operation period, System uptime is the total time that the system is operating, and System downtime is the total time that the system is not operating. A conservative estimation showed that the required steady-state availability for the JAEA-ADS project is 0.998. This result was computed using the values of Table I in Eq. (3). The Total time is 7200 h, and the System downtime is the only contribution of beam trips longer than 10 s, assuming the shortest beam trip duration for each of the categories.

Table III presents a simple estimation of the steady-state availability of the JAEA-ADS linac is enhanced by increasing the number of elements that can be compensated simultaneously. The straightforward calculation considered only the SRF cavities. The same equations were used because the reliability and availability have the same representation for those configurations. We assumed that each SRF cavity has a high availability of 0.999. For series configuration, Eq. (2) is used. For *n-1-out-of-n* configuration, i.e., the linac only needs 292 of its 293 SRF cavities to operate. Similarly, the *n-5-out-of-n* configuration means the linac can operate using only 288 of its 293 SRF cavities. The last two configurations applied Eq. (1). The system satisfied the required availability by increasing the number of elements, which were compensated simultaneously. Of course, this is a simple and optimistic estimation, so a more detailed assessment is undergoing.

The *k-out-of-n* redundancy was implemented by applying local compensations that exploit the linac modularity by

TABLE III. Simple steady-state availability estimations for the main linac of the JAEA-ADS accelerator, for series and *k-out-of-n* configurations.

SRF section	Number of SRF cavities (n)	Series	*n-1-out-of-n*	*n-5-out-of-n*
Main linac	293	0.746	0.965	0.999

using the nearby Non-Faulty element to compensate for the unwanted effect of the Faulty element. This enables a fast beam recovery by readjusting only the components around the affected region. Consequently, the scheme complexity and beam mismatch [18], which is one of the primary sources of beam degradation, are reduced. Nevertheless, the compensation efficiency decreases when the beam energy is small, early in the linac. In addition, the readjusted devices are exposed to higher operational stress than in regular running, which could lead to a malfunction.

This work focused on testing the feasibility of local compensations for the principal components of the linac, i.e., SRF cavities and magnets. We analyzed single independent failures in SRF cavities, multiple SRF cavity failures, and magnets. This study aims to develop a local compensation procedure and create a Faulty-element database that will be tested and updated during the beam commission. The application of the local compensation scheme is expected to take < 10 s in our case to make it appropriate for our operation to aim to reduce the trips whose duration is longer than 10 s, which are shown in Table I.

Figure 3 presents the flowchart for the development of these schemes. The retuning of the lattices was done using TraceWin [19]. TraceWin can readjust the parameters of the SRF cavities and magnets to achieve a target beam value, i.e., a certain desired beam energy, at a given position by adding an ADJUST command before the retuned element and a DIAGNOSTIC element at the place at which the desired beam value is located. The DIAGNOSTIC element measures a specific beam property such as beam energy, beam phase, transverse root-mean-square (rms) beam size, transverse beam centroid, beam Twiss parameters and compares the measured value against the target value. For the local compensation of the JAEA-ADS linac, the DIAGNOSTICS of energy, phase, Twiss parameters, and beam size were employed, as shown in Fig. 4. The parameter of the associated component is tuned until the quadratic sum of the differences between the measured and the wanted beam value divided by the wanted one reaches the limit criterion or when the number of iterations exceeds the maximum value. In each compensation, the used DIAGNOSTICS elements for the retuning were at the end of the most downstream readjusted element period. However, for magnet compensation, the employed DIAGNOSTIC for the beam size was the nearest to the Faulty magnet. The maximum acceptable accuracy for the DIAGNOSTIC was the order of mdeg for the phase, keV for the energy, 100 μm for the beam size, and 10^{-2} for the Twiss parameters.

Figure 4 shows the local compensation scheme for a Faulty-SRF cavity, but the compensation for a Faulty magnet is similar. Achieving a proper compensation for a Faulty-SRF cavity will require reaching the synchronization between the retuned area with the rest of the linac.

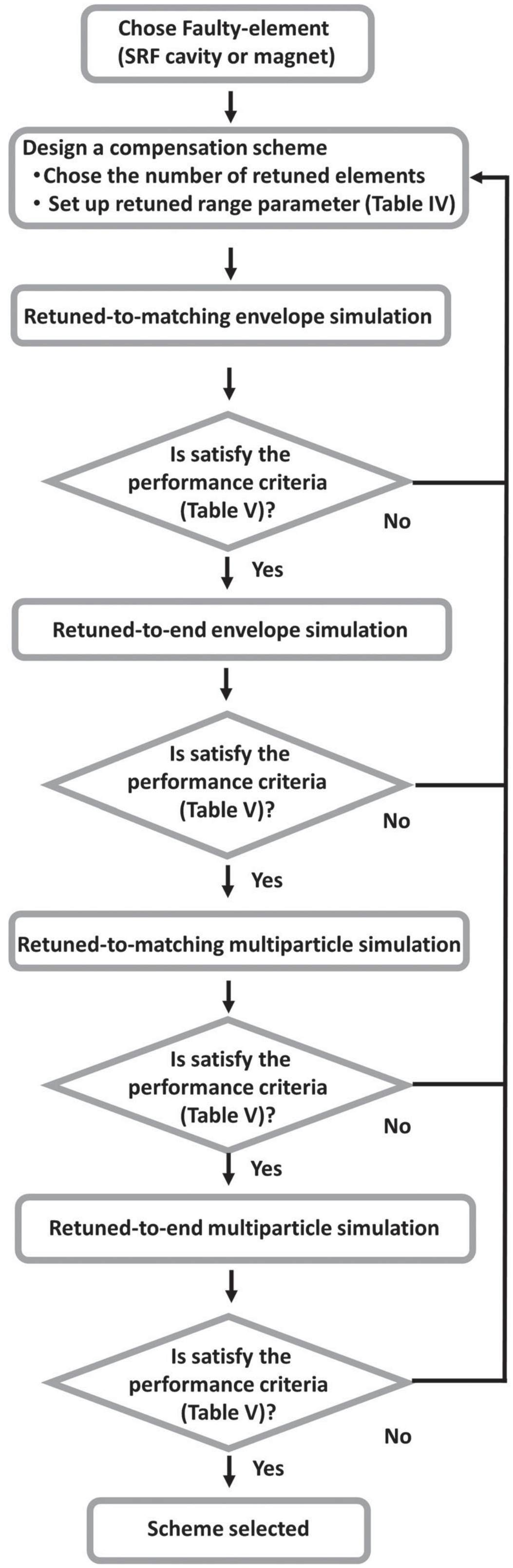

FIG. 3. Flowchart to implement local compensation schemes.

Thus, no rebunching in the downstream SRF cavities will be needed. In the linac, all the SRF cavities are synchronized regarding the absolute rf phase (ϕ). ϕ is associated

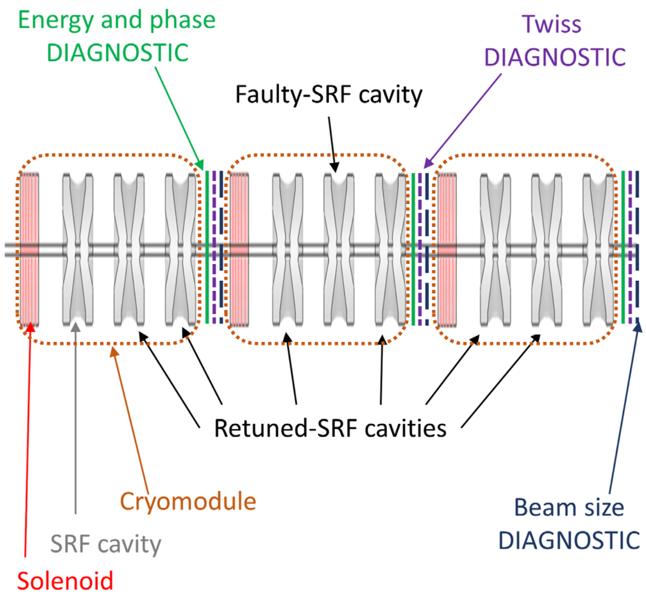

FIG. 4. Local compensation scheme. The failure in the middle SRF cavity of the SSR2 section. The nearby SRF cavities, the number of elements depending on the working point, were used to restore the energy and beam phase at the beam diagnostics located at the end of the period of the last upstream retuned elements. In some cases, the magnets associated with the retuning cavities are readjusted to reduce beam mismatch.

with the time of flight of the beam in the linac and is represented as

$$\phi = \frac{2\pi}{\lambda}\int_{s_0}^{s_0+s}\frac{ds'}{\beta(s')}, \tag{4}$$

where s_0 is the start point and s is a certain downstream point where the ϕ is calculated, λ is the rf wavelength, $\beta = v/c$ is the baseline beam velocity reduced.

In the Faulty-SRF cavity case, the missing energy gain changes the ϕ producing phase slip [13,20]:

$$\delta\phi = \frac{2\pi\Delta s}{\lambda}\frac{\delta\beta}{\beta^2}, \tag{5}$$

where Δs is the distance from the Faulty-SRF cavity and $\delta\beta$ is the change of beam velocity due to the failure. Phase slip will affect the final beam energy and, if the value is large, will drive the beam out of the stability region, causing significant beam degradation and beam loss. Therefore, the primary goal of the Faulty-SRF cavity compensation is to restore the baseline beam energy and phase at a certain downstream point, which is indicated by a DIAGNOSTIC element, where the failure is located. The compensation is achieved by adjusting E_{acc} and ϕ_s of the nearby Non-Faulty-SRF cavities, but these changes could affect the beam performance inducing beam mismatch. Therefore, a small readjustment in E_{acc} and ϕ_s for SRF cavities and magnetic field for the magnets are applied to achieve beam Twiss parameters similar to the baseline at the energy restore location, using the elements closest to the restore point.

With the magnets, a failure will cause an uncontrollable transverse beam envelope growth that results in considerable beam loss, affecting the integrity of the linac and the required beam power. Thus, the principal aim of the Faulty-magnet compensation is to control the transverse envelopes in the affected zone and restore their behavior at a downstream point by changing the fields of the magnets and parameters of the SRF cavities when it is necessary.

The compensation depends on the operating points in which it takes place. Consequently, the number of readjusted elements varied throughout the linac. As a trade-off between achieving acceptable performance and reducing the complexity of the compensation scheme, we chose a maximum of 25 readjusted components for single failures and 40 for multiple failures. However, it is worth mentioning that the Multi-purpose Hybrid Research Reactor for High-tech Applications (MYRRHA) project has recently implemented a compensation using all the cavities of the SRF, known as global compensation [21]. The global compensation shows the advantages of simultaneously compensating several SRF cavities, but its complexity is greater than the local one. Recently, we have started regular discussions with the MYRRHA team about local and global compensation methods for ADS linac.

Table IV presents the range of the readjusted values. The constraints were set to reduce operation stress in the retuned components and sustainable beam operation. E_{acc} increase was limited to 20% above the baseline operation to ensure a maximum electric peak surface field of 36 MV/m inside the SRF cavity to keep the operational stress tolerable. The allowable change of ϕ_s is about 50% of design values to avoid dangerous longitudinal acceptance reduction. In particular, the ϕ_s retuned interval setting for the low-energy, nonrelativistic, SRF cavities is critical because the phase slip in the downstream SRF cavities increases significantly. Thus, we choose the limits of the ϕ_s interval based on some rough estimates using Eq. (5) that were corrected through various simulation interactions. In addition, we also monitored the readjusted beam power of the cavity. Figure 5 presents the cavity beam power and the magnetic field for the main linac of the JAEA-ADS baseline operation and the considered limits for the compensation. For the cavity beam power plot, the limit depends on the retuned E_{acc} and ϕ_s; therefore, only as a reference, we plotted the maximum limit of retuned 30%

TABLE IV. Retuned tune parameters constraints.

Parameters	
Maximum E_{acc}	$\leq$ 20% of the baseline design
Maximum $\Delta\phi_s$	$\leq$ 50% of the baseline design
Maximum magnetic field	$\leq$ 8 T for superconducting solenoids
	$\leq$ 1.8 T for normal quadrupoles

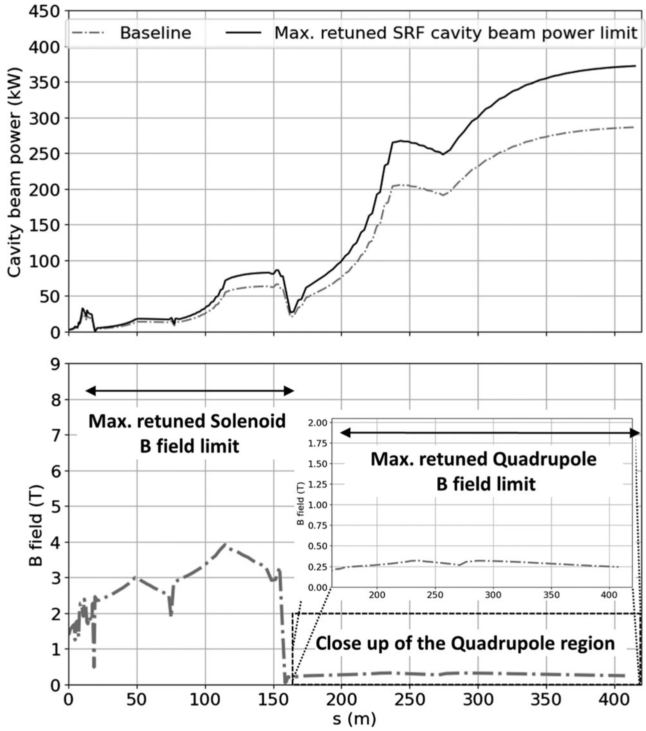

FIG. 5. Cavity beam power (top) and the magnetic field (bottom) at the main linac. On the magnetic field plot, a close view of the quadrupole region is included.

higher than the baseline, which agreed with the results present in Sec. III.

For magnets, the upper limit of the retuned parameter was less stringent. Present superconducting solenoids have achieved magnetic fields greater than 8 mT [22], and for the quadrupoles, the magnetic field at the plot tip must be below 1.8 T to ensure the operation with normal conducting magnets. Those limits are far from the magnetic field operation, providing more flexibility to select retuned values; however, we pursued operating with low retuned magnetic fields to reduce costs. Each solenoid and doublet quadrupole is fed up with independent power supplies to allow field adjustment.

Each scheme comprised two types of simulations: envelope and multiparticle. Additionally, each of the simulations consisted of two-step tracking: retuned-to-matching, i.e., a few periods around the Faulty elements where the retune and matching were done, and retuned-to-end, which is from the rematched lattice to the end of the linac. We chose this route because envelope simulations provide fast and reliable solutions to select possible compensation schemes that are then accepted or rejected through multiparticle simulations. In the same vein, retuned-to-matched simulations allow early detection of any beam degradation. It is noteworthy that the retuned parameters took place in the retuned-to-matching envelope simulation. The other simulations only evaluated whether the readjusted scheme meets the conditions.

TABLE V. Beam performance criteria for the multiparticle simulations.

Parameter	Retuned-to-matching	Retuned-to-end
Total beam loss[a] (%)	< 0.1	<1
Maximum power loss[a] (W/m)	<1	<1
$\Delta E/E_0$ (%)	<0.5	<1
Transverse $\Delta\varepsilon/\varepsilon_0$[a] (%)	<15	<30
Maximum transverse size[b] (3σ)	<aperture	<aperture
Transverse beam mismatch	<0.10	<0.25
Longitudinal beam mismatch	<0.15	<0.30

[a]Only for multiparticle simulations.
[b]Only for envelope simulations.

The accepted compensation schemes satisfied the criteria presented in Table V according to the type of simulation. The criteria are mainly based on the requirement of retuned-to-end multiparticle simulations, which are the final criteria of acceptance. The total amount of beam loss must be lower than 1% for beam window integrity [23]. In addition, the local power loss must be < 1 W/m to ensure hands-on maintenance. The energy difference ($\Delta E/E_0$) of the retuned lattice to the baseline must be below 1% to be acceptable for the beam window. Beam dynamic studies of the JAEA-ADS BTT [24] showed that input beams, i.e., the beam distribution at the end of the linac, with transverse rms emittance growth (transverse $\Delta\varepsilon/\varepsilon_0$) larger than 30% and a transverse beam mismatch, as is defined in the Appendix A, larger than 0.25, and a longitudinal beam mismatch larger than 0.3 to the baseline design changed the transverse beam size. As a result, the percentage of the scraped beam in the BTT was varied, resulting in beam power fluctuations beyond the acceptable $\pm 1\%$ [23]. Furthermore, the changes in the transverse beam profile at the beam window alter the current density, which will induce thermal stress that compromises the integrity of the beam window. Thus, we set the tolerable transverse rms growth to be $< 30\%$ and the transverse and longitudinal beam mismatches to be less than 0.25 and 0.3, respectively.

III. FAULT TOLERANCE STUDIES

The main linac of JAEA ADS is composed of 293 SRF cavities and 153 magnets; thus, the testing for each element will require a considerable amount of time and computational resources. Figure 2 shows that the main parameters of the SRF cavities have an increased tendency, with saturation, or slightly decreased at the end of each section. For the magnets, the magnetic fields follow a kind of inverted v-shape, i.e., an initial increase until a maximum and then a decrease, as is presented in the bottom plot of Fig. 5. Thus, to elude a long time-consuming simulation campaign but still simulate enough cases to explore all the parameter ranges, we analyzed all the SRF cavities and magnets at the beginning, middle, and end of the periods of the different SRF sections.

A. SRF cavity failures

1. Single SRF cavity failures

The first case analyzed was the compensation of single SRF cavity failures because the SRF cavities are the most frequent elements in the linac and also the most prone to problems; thus, this scenario is the most probable to happen [10,13–16,25]. As it was explained above, the energy recovery was accomplished by adjusting E_{acc} and ϕ_s of the Non-Faulty element. The readjusted values had a significant impact on the longitudinal acceptance. Consequently, the selected values also seek to lead to a tolerable acceptance reduction.

We decided only to apply for local compensation from the SSR1 section for the following because the effectiveness of the compensations decreased at low energies because of the space charge and nonlinear components of the rf [26] induced beam degradation. In addition, based on other ADS linacs [13,14], local compensations are more suitable for energies higher than 10 MeV.

Figure 6 presents E_{acc}, ϕ_s, and the beam energy for the baseline design and the compensation of the SRF cavity 163, the last of the SSR2 section, as an example. In this case, the scheme comprises seven SRF cavities: three upstream and four downstream. The failure was simulated by setting the values of the Faulty-SRF cavity to zero, as shown in Figs. 6(a) and 6(b). Figure 6(c) presents an increase in the beam energy of the compensation scheme to the baseline from the first retuned SRF cavities. Then, the energy remains the same until the nearest downstream SRF cavity of the Faulty element, which emulates the nonenergy gain effect due to the Faulty-SRF cavity. Finally, the beam energy is increased in the downstream part until the baseline energy is recovered. Figure 6(d) shows the ϕ difference between the baseline and the retuned scheme, $\Delta\phi = \phi_{\mathrm{baseline}} - \phi_{\mathrm{retuned}}$, obtained from the simulations. Please note that $\Delta\phi$ is equivalent to $\delta\phi$ defined in Eq. (5), but not strictly the same. In the initial part, the energy gain of the retuned scheme is larger than the baseline, i.e., β is higher; therefore, the absolute phase difference is positive. The difference increases until the location of the Faulty cavity, then, it decreases and becomes zero at the end of the retuned section. Thus, the retuned scheme reached synchronization with the rest of the linac.

Figure 7 compares the results of multiparticle simulations between the baseline and retuned lattice. The simulations were performed from some periods upstream of the Faulty-SRF cavity until the end of the linac since this is the region that would be affected by the retuning. Top and bottom plots of Fig. 7 exhibit that the transverse plane for both cases is almost the same. In the middle plot of Fig. 7, the change in phase and acceptance caused by the compensated scheme is observed, resulting in small growth in the final longitudinal emittance of 7.6% to the baseline, as shown in the bottom plot of Fig. 7. However, the phase envelopes remain similar to the baseline.

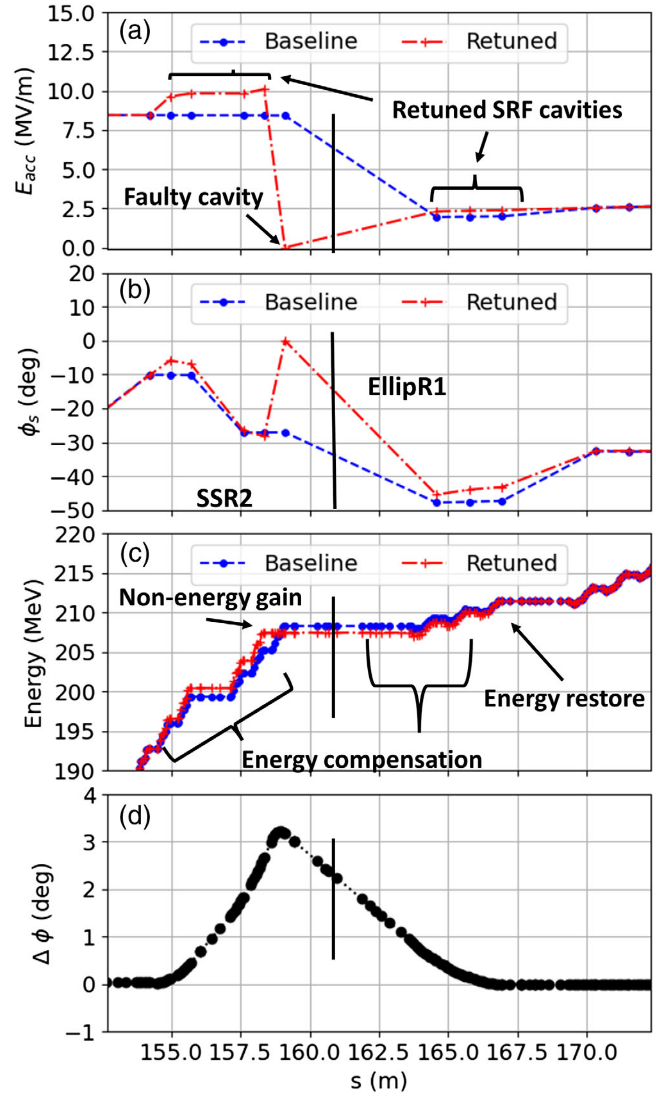

FIG. 6. Accelerating gradient (a), synchronous phase (b), beam energy (c), and the difference in absolute rf phase (d) for the compensation scheme of the failure in the last SSR2 cavity. Please note that s is the distance from the main linac entrance.

Table VI in Appendix B summarizes the compensation schemes, including the retuned elements, and beam output performance. As we expected, the maximum beam degradation for single SRF cavities was set for the performance in the SSR1 region. No beam loss was recorded. The transverse rms emittance growth was below 4% regarding the baseline, and the longitudinal emittance growth was lower than 23%. The low-energy sections, SSRs, and the transition regions presented the largest emittance growth, especially in the longitudinal plane. In addition, a significant emittance growth was recorded in the middle of the EllipR1 section caused by the strong coupling of the transverse planes. The beam mismatch was reduced to

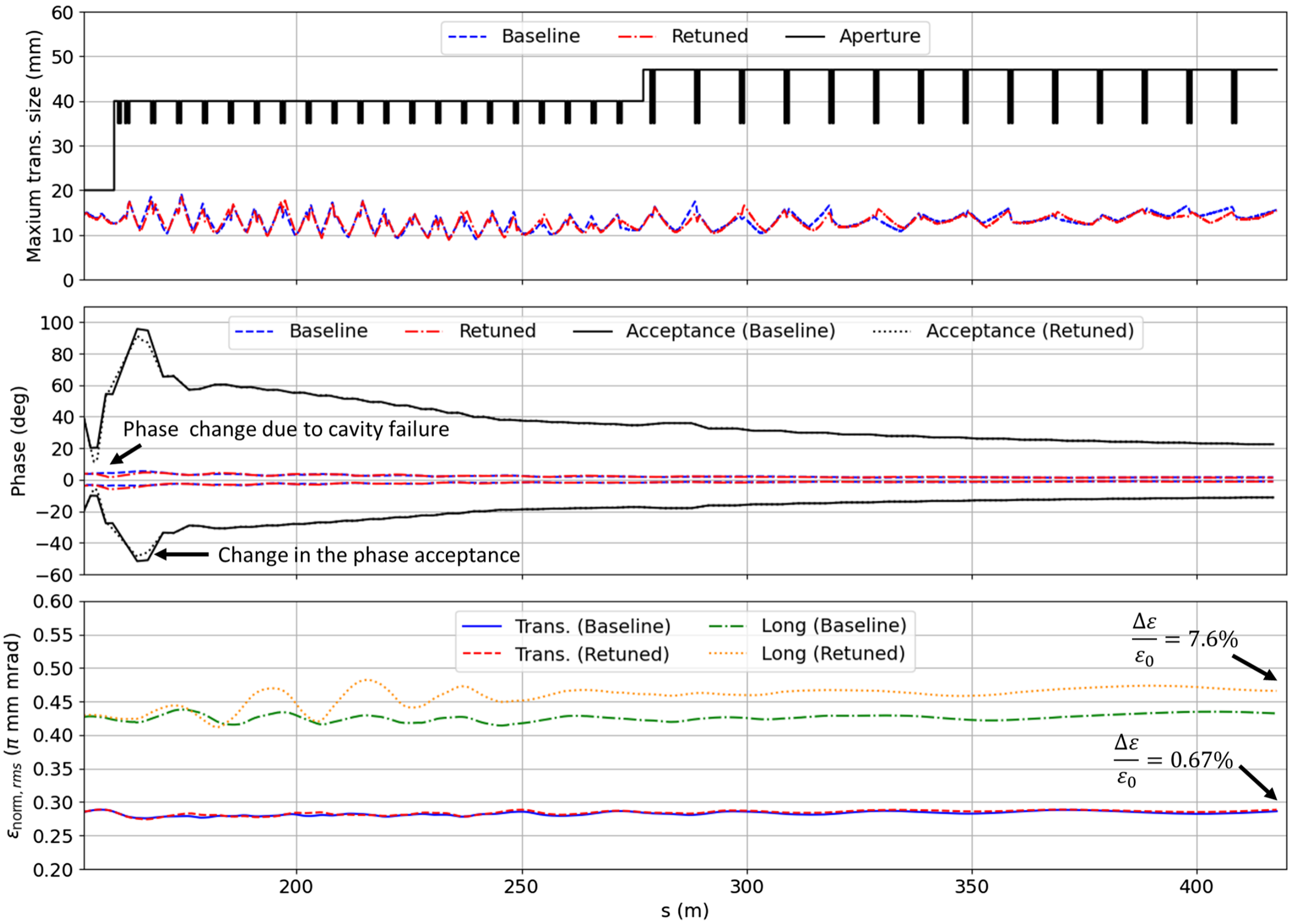

FIG. 7. Comparison of the beam envelopes and normalized rms emittance between the compensation scheme of the failure in the last SSR2 cavity and the baseline. Please note that s is the distance from the main linac entrance.

0.01 in all the planes. The energy difference was below 0.02% for all the analyzed cases, and the maximum power increase of a retuned element was lower than 30% of its baseline value. For the most demanded rf power case, end of the EllipR2 section, the cavity power required was 347 kW, which is 20% higher than its baseline value. In addition, the maximum magnetic peak for the SSR cavities was 50 mT and for EllipR was 70 mT.

The beam simulations showed that magnet retuning was not required for the compensation because the beam performance using only SRF cavities was enough to fulfill the criteria of Table V. Moreover, it is desirable to readjust the minimum number of elements to reduce the complexity of the scheme. The average numbers of retuned SRF cavities were six. The negative values of the emittance growth mean that the emittance was reduced with respect to the baseline value.

2. *Multiple SRF cavity failures*

We pursued our linac can accept simultaneous SRF cavity failures to enhance the reliability. Besides, a failure in one element could affect the other SRF devices that share the same cryomodule. Thus, we investigated multiple Faulty-SRF cavities that simultaneously occurred. The study was conducted by analyzing two scenarios: multiple Faulty-SRF cavities in independent periods and Full-Period (FullPer), e.g., all the SRF cavities that composed a single lattice period. For the study of multiple Faulty-SRF cavities in independent periods, we evaluated the case of failures in each section, from SSR1 to EllipR2. The first cavity of SSR1 and the final cavities of each SRF region were assumed faulty because the SRF elements around the transition zone play a fundamental role in the linac performance. Moreover, the SRF cavities in the last period of each SRF section operate with higher E_{acc} than the ones in the first period of the following section, as shown in the top plot of Fig. 2. The scheme was based on the studies for a single Faulty-SRF cavity.

Figure 8 presents the retuned E_{acc}, ϕ_s, and the difference in the absolute phase for multiple SRF cavity failures. In Appendix B, the result in Table VII shows an efficient beam performance, except for the longitudinal emittance growth and beam mismatch. The failure at the beginning of SSR1 was the principal source of the significant longitudinal beam degradation, and the downstream failures aggravated the beam performance, resulting in a considerable emittance growth. However, the longitudinal acceptance preserved, white area, was about 3 times the 99% of the input longitudinal emittance ($\varepsilon_{\mathrm{norm},z,0}$) as shown in Fig. 9. The compensation scheme, which consists of independent rematches based on the single SRF cavity compensations, is reported in Table VI.

In the FullPer cases, we simulated the failure of all the SRF cavities that composed one whole individual period each time, and the Faulty periods were selected following the same criteria as the multiple Faulty-SRF cavities in independent periods. The schemes required the readjustment of about two to three periods before and after the faulty one, except for the first period of SSR1 and the last of EllipR2, which used two periods downstream and five periods upstream, respectively. As it was pointed out for the single failures, the retuned E_{acc} and ϕ_s must be done carefully. The ϕ_s readjustment was more challenging than the previous case because the phase slip was considerable due to the significant energy change. Each SRF-cavity's ϕ_s was adjusted in succession to achieve an acceptable value. In most cases, the simulations showed that magnet retuning improved the beam performance.

Figure 10 presents the compensation scheme for the failure of all the SRF cavities in the first SSR1 period (FullPer I). The four downstream SRF cavities were retuned to achieve the compensation in energy, as shown in Figs. 10(a)–10(c). Similar to Fig. 6(d), Fig. 10(d) shows that the synchronization with the downstream is achieved by making $\Delta\phi$ to zero at the end of the retuned section.

Figures 11–13 show the beam density for the baseline case and the failure of all the SRF cavities of the first SSR1 period without and with compensation (FullPer I), respectively. FullPerI case presented the greatest degradation of the beam parameters among all the compensations. If all the SRF cavities of the first cryomodule of SSR1 failed, Figs. 12(c) and 12(d) show a smooth escape of a tiny fraction of the beam from the zone of stability in the longitudinal plane. Consequently, most of the beam was transported, as presented in Figs. 12(a) and 12(b). Only a small beam fraction, about 0.1%, reached the beam apertures around the transition between different SRF sections. However, Fig. 12(e) exhibits beam losses greater than 100 W/m in the EllipR2 section.

In our lattice, the first SSR1 cryomodule is used mainly for the longitudinal matching with the HWR section and provides a small energy gain of 0.4 MeV; thus, the $\delta\phi$ was tiny. Therefore, the effect in the beam lattice was small, allowing the transport of most of the beam through the linac. For a failure in all the SRF cavities in the last period of SSR1, which was equivalent to the Fullper II case without compensation, the energy loss was 1.6 MeV, almost 4 times the energy provided by the first SSR1 cryomodule. The $\delta\phi$ was bigger, making the beam became lost before reaching the last SRF section. In the SSR1 section, a failure in all the SRF cavities of the last cryomodule became more dangerous

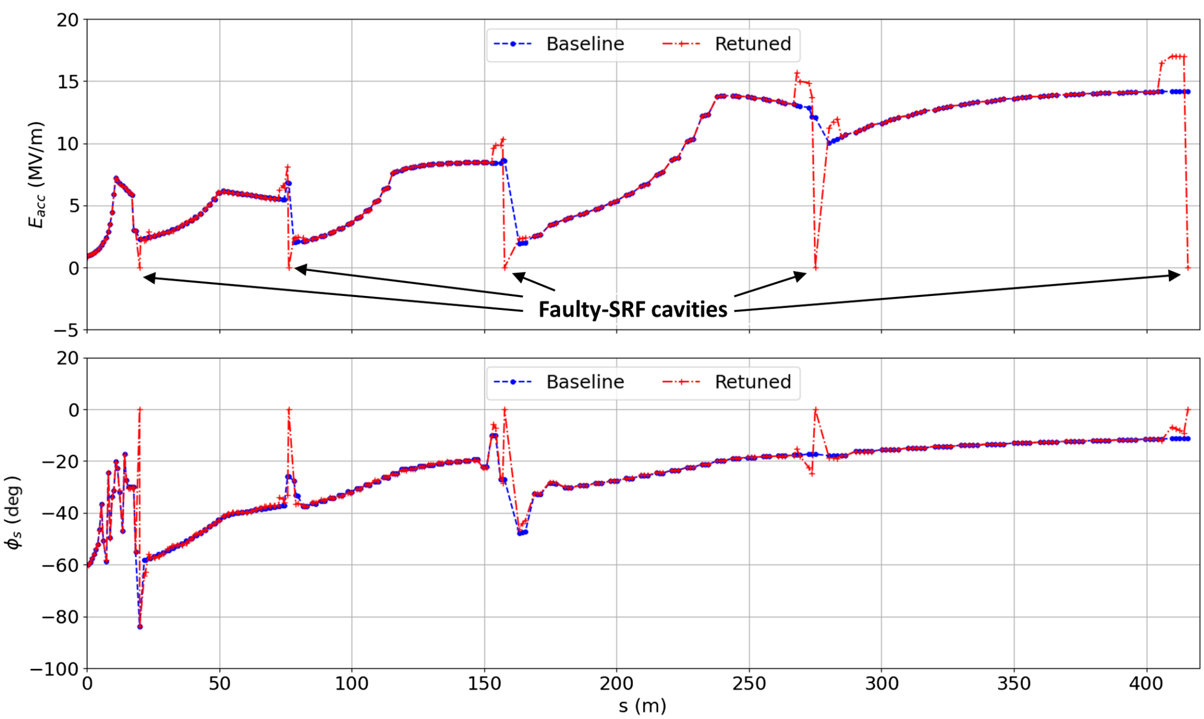

FIG. 8. E_{acc} (top) and ϕ_s (bottom) plots for multiples SRF cavity failures in independent periods.

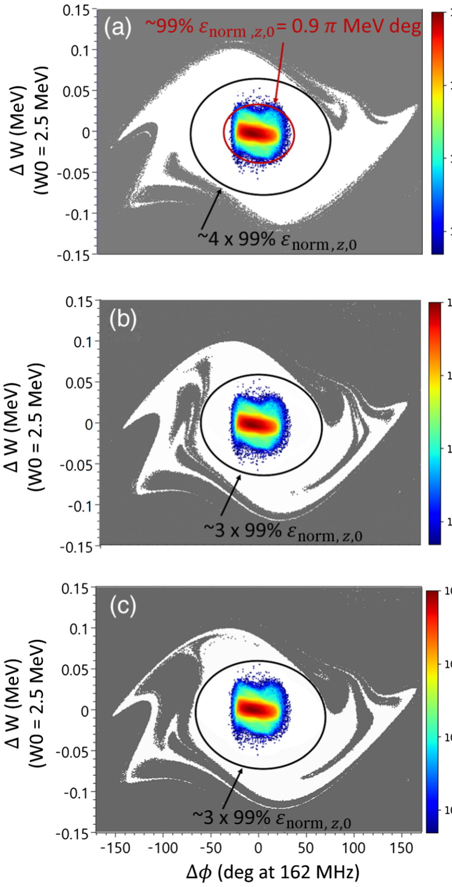

FIG. 9. Longitudinal acceptance at the entrance of the main linac for the different cases: baseline (a) [7], multiple SRF cavity failures in independent periods (b), and failure in the first SSR1 period, known as FullPer I, (c). The input longitudinal emittance is plotted as a reference in each subplot. In subplot (a), the solid red ellipse represents 99% of the input longitudinal emittance ($\varepsilon_{\mathrm{norm},z,0}$), 0.9 π MeV deg. In each subplot, the solid black line is the maximum fittable ellipse inside the acceptance. The black ellipse corresponds to approximately 4 times 99% $\varepsilon_{\mathrm{norm},z,0}$ for the baseline and 3 times for the failure cases.

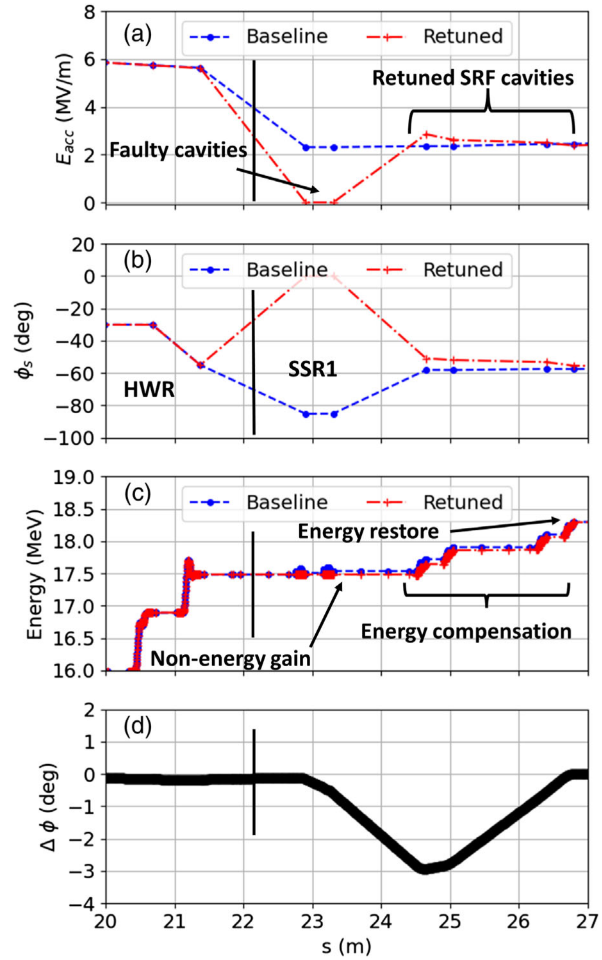

FIG. 10. Accelerating gradient (a), synchronous phase (b), beam energy (c), and the difference in absolute rf phase (d) for the compensation scheme of the failure in the all the SRF cavities of the first SSR1 period (FullPer I). Please note that s is the distance from the main linac entrance.

than in the first cryomodule. The reason was that $\delta\phi$ was larger because the energy gain increased toward the end of SSR1. However, achieving proper compensation is more difficult at the beginning than at the end of the SSR1, as shown in Table VII.

The comparison of Figs. 11 and 13 shows that the compensation scheme effectively managed the envelopes of the beam. Figure 13(c) shows some oscillations in the phase, and Fig. 13(d) reveals the energy dispersion is slightly increased. However, the longitudinal parameters remain acceptable.

In addition, Fig. 9 compares the longitudinal acceptance at the entrance of the main linac for the baseline against multiple Faulty-SRF cavities in independent periods and the FullPer I. For the failure cases, the acceptance area was reduced by approximately one quarter regarding the baseline. However, the remaining acceptance was approximately 3 times the 99% of the $\varepsilon_{\mathrm{norm},z,0}$. It is worth mentioning that, for multiple Faulty-SRF cavities and FullPer I, the longitudinal acceptance was similar; thus, the failure of the first SSR1 cavity was mainly responsible for the acceptance reduction. Additionally, Fig. 14 contrasts the phase-space distribution of the baseline case against the FullPer I. The total transverse emittances did not record a significant increase, but it is seen that the particle density increased out the core, yellow-green surface, which results in more dense tails. On the contrary, the emittance growth on the longitudinal plane was notable, but it was acceptable.

The results of the multiple SRF cavities failures are reported in Table VII. Similar to the single SRF cavity cases, the beam performance of the compensation schemes decreases toward low-energy sections; thus, the maximum beam degradation was established for the results of SSR1. However, it is noteworthy that the largest emittance growth corresponds to the frequency jump region, from HWR to SSR1 and SSR2 to EllipR1. The overall beam performance

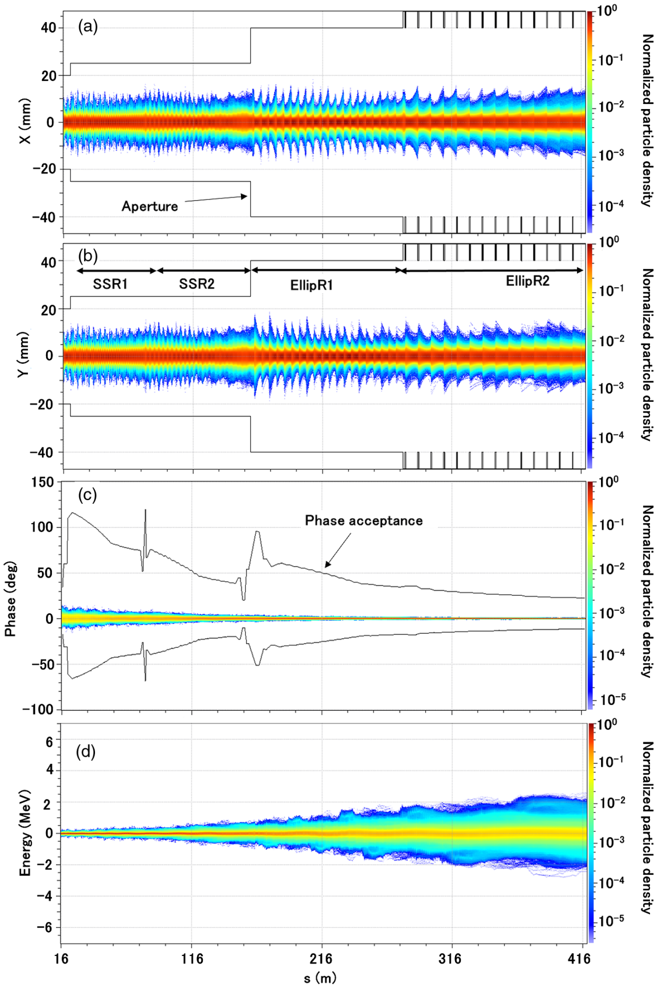

FIG. 11. Beam densities of the baseline case: horizontal (a), vertical (b), phase (c), and energy (d). Please note that s is the distance from the main linac entrance.

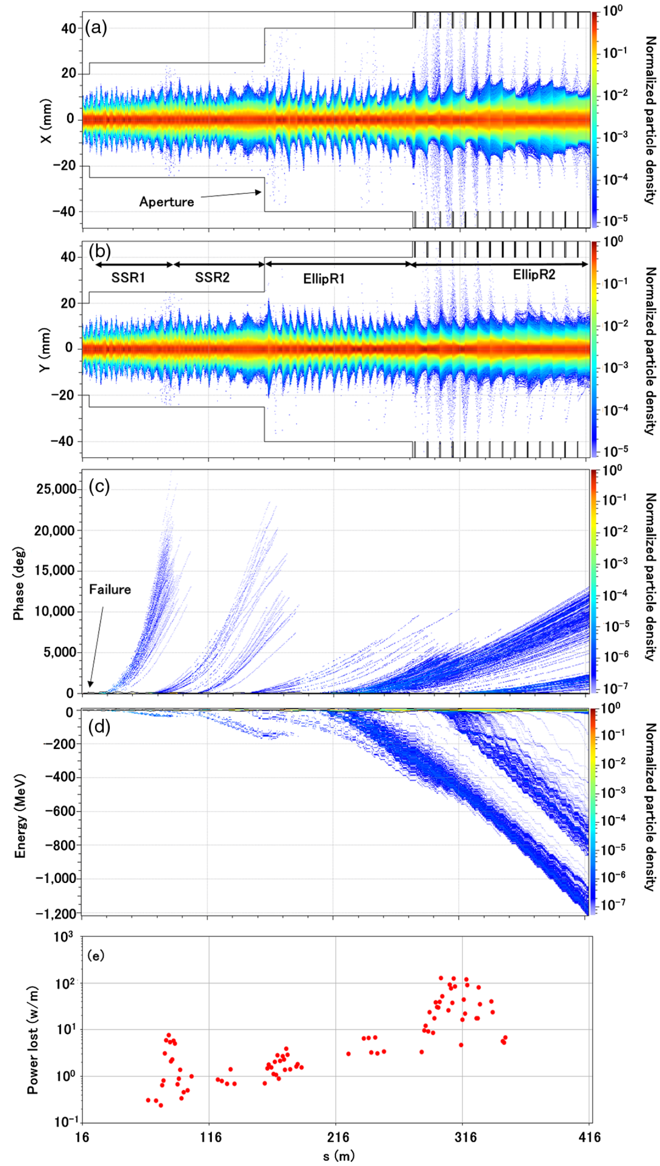

FIG. 12. Beam densities and power lost distribution for a failure in all SRF cavities in the first period of SSR1, which is equivalent to the Fullper I case without compensation. Subplots (a), (b), (c), and (d) are the horizontal, vertical, phase, and energy densities, respectively. Subplot (e) is the power lost distribution. Please note that s is the distance from the main linac entrance.

was acceptable without beam loss. The energy difference was lower than 0.02%, the transverse parameters were close to the single failures, and the maximum retuned cavity power and magnet were feasible with present technology.

There was a significant degradation of the longitudinal parameters, especially in the emittance growth. However, that outcome did not enhance the beam loss because the baseline model was optimized to have a broad longitudinal acceptance to deal with the longitudinal acceptance reduction due to compensation schemes, as shown in Fig. 9. Thus, the results showed that the compensation of multiple SRF cavities that composed individual periods could be applied in the EllipRs and SSRs sections.

B. Magnet failures

For the failure in the quadrupole, it is advisable to turn off the whole doublet to avoid significant beam mismatch for the downstream sections [13,27]. This strategy was applied only to the EllipR section. Figure 15 shows the retune on the solenoid's magnetic field at the top and the SRF cavity's ϕ_s in the middle for a failure of the solenoid 41, the middle period of SSR1. The compensation scheme comprised seven magnets and eight SRF cavities. The parameters were retuned to control the transverse envelope growth because of the missing solenoid, as shown in the bottom plot of Fig. 15. In this scheme, the SRF cavities near the faulty solenoid were retuned to control the beam envelope; therefore, two downstream SRF cavities were rematched to compensate for any energy change due to the upstream readjusted SRF cavities.

Table VIII in Appendix B shows the relevant results of this study. The magnetic field plotted in the bottom plot of

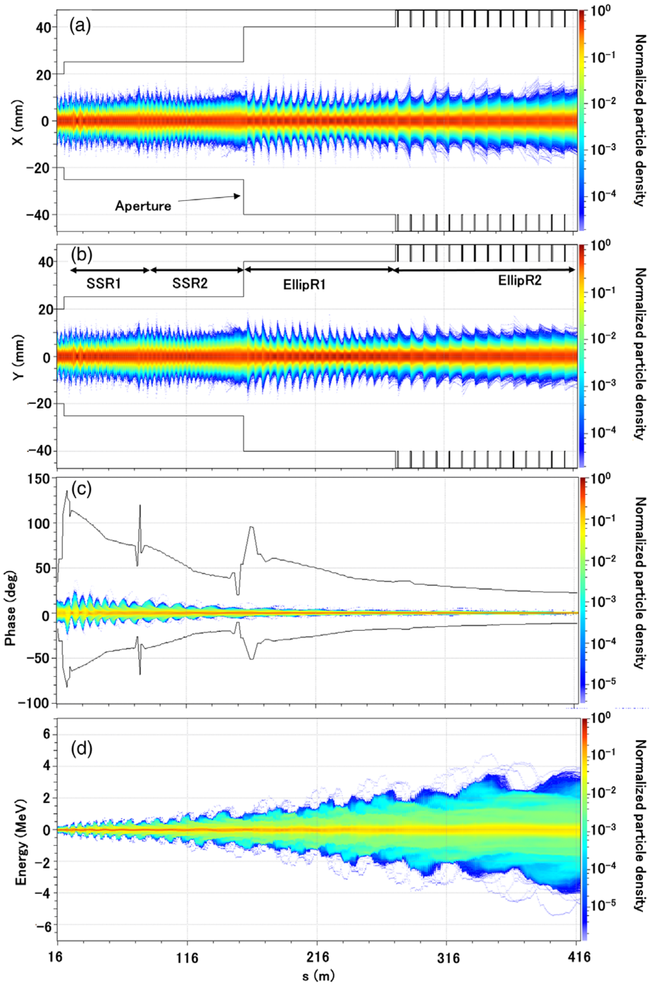

FIG. 13. Beam densities of the compensation scheme for FullPer I case: horizontal (a), vertical (b), phase (c), and energy (d). Please note that s is the distance from the main linac entrance.

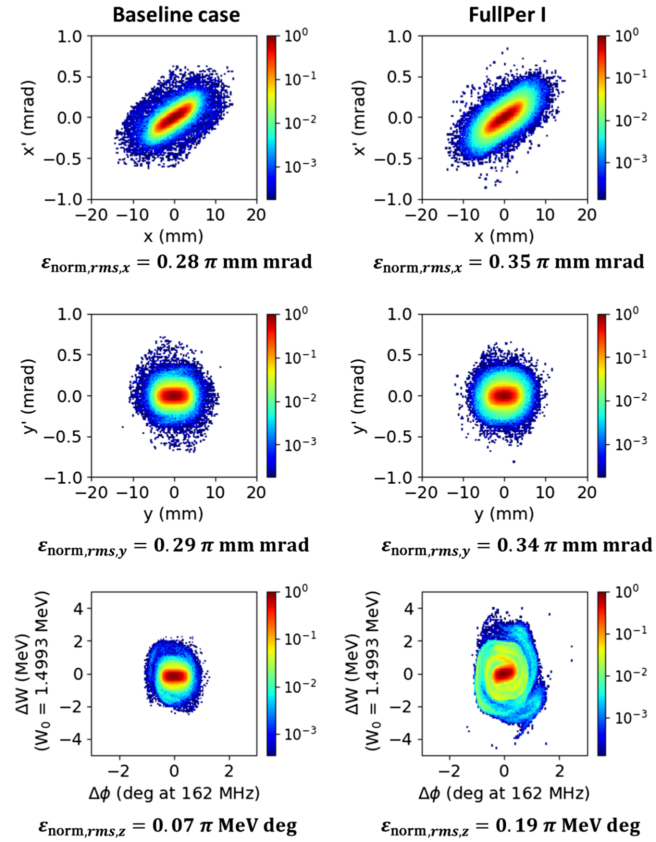

FIG. 14. Comparison of the phase-space distribution between the baseline case (left) against the compensation scheme for the failure in all the SRF cavities of the first SSR1 period (right) at the end of the linac.

Fig. 4 helps us understand the outcome of these compensations. The magnetic field at the end of each SRF section is smaller than the first period of the following region to achieve an appropriate transverse matching. In addition, the maximum field is in the middle of the SSR sections. However, for the EllipR1, the maximum is slightly toward the end, and for the EllipR2, the maximum is at the beginning. Thus, there is a correlation between high magnetic fields and lower compensation beam performance. The poor performance came from a failure in the middle of EllipR1 due to the strong transverse coupling and high magnetic field, i.e., the corresponding quadrupole gradient of 8 T/m. It is worth mentioning that the frequency jump regions had moderate performance, except for the longitudinal emittance growth at the transition of HWR to SSR1. In the second frequency jump, SSR2 to EllipR1, the extra two quadrupoles employed for the matching were crucial to restoring the beam parameters for failures around that region. The highest percentage increases, about 3 and 5 times the baseline value, occurred in the extra matching magnets at the frequency jump regions.

Beam loss was not recorded. The rms emittance growth remained under 25% in all the planes, beam mismatches were lower than 0.15, the energy difference went up to 0.01%, and the maximum values of the retuned cavity and magnets were below the operating limits. The ratio of the aperture to the maximum transverse size was computed to check the safe margin of retuned schemes. For the baseline case, the minimum ratios were 1.25 and 2.0 for the SSR and EllipR sections, respectively. The ratios were computed only for magnet failures because the beam envelopes were almost unaffected by the SRF cavity failures. The minimum ratios were large in the EllipR sections than in the SSR ones, but the minimum was recorded in the middle of the EllipR1 section, which also presented the highest transverse emittance growth. By comparing against the baseline, the ratios at the EllipR had the largest reduction. The reason was that the distances between Faulty and Non-Faulty components were longer for the EllipR section than for the SSR part; therefore, the transverse envelopes were controlled by the retuned elements early in the SSR region before their envelope sizes increased significantly.

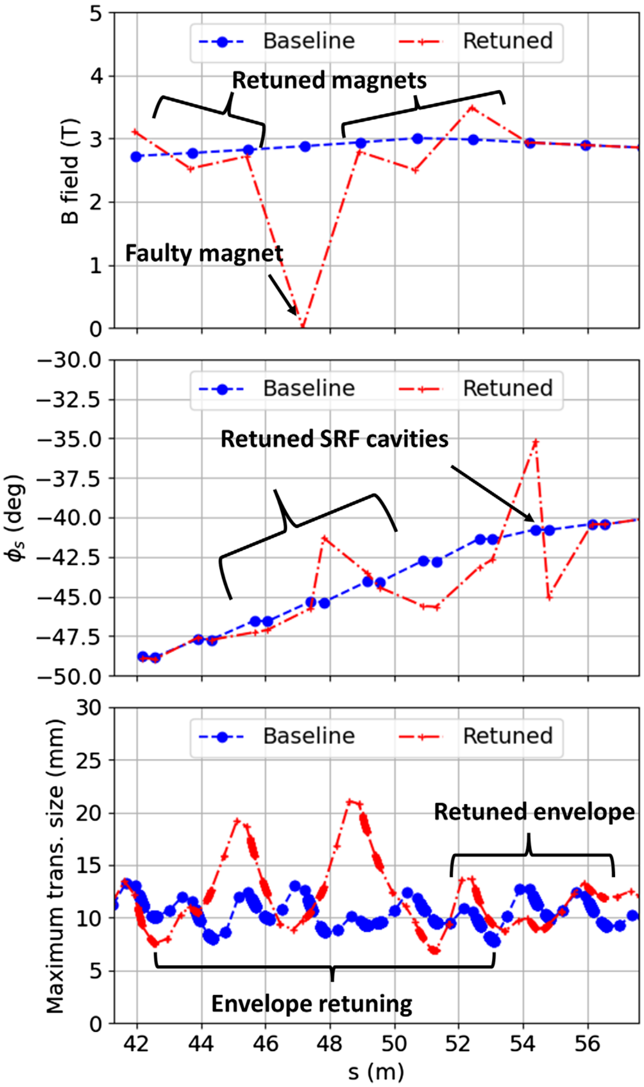

FIG. 15. Retuned elements and beam envelope for the compensation scheme of the failure of the solenoid in the middle part of the SSR1 section. Please note that s is the distance from the main linac entrance.

IV. CONCLUSIONS

The reduction of beam trip duration is one of the key strategies to reach the demanded reliability of the ADS linac; thus, we explored the tolerance of the linac lattice for the local compensations for fast beam recovery. The results showed that the JAEA-ADS linac could efficiently handle single SRF cavity, magnets, and simultaneous SRF cavities failures from the single-spoke region to the end of the linac. In particular, the compensations of simultaneous SRF cavities that compose whole individual periods were the most advanced and relevant results of this study.

The rematched schemes did not produce extra-beam loss, and the difference between the final energy and the transverse rms emittance to the baseline was less than 0.02% and 23%, respectively. Moreover, the resulting beam mismatches, below 0.23 in all the planes, together with the above beam performance, provided acceptable beam input conditions for the beam transport to the target line to satisfy the beam stability at the beam window and the target.

In addition, the maximum retuned element parameters were carefully selected to guarantee tolerable operation stress. The electric field in the SRF cavity was up to 36 MV/m, and a feasible operation within the capability of the present systems, a maximum required rf power of 77 kW for single-spoke SRF cavities and 374 kW for ellipticals. The maximum rematched magnetic field for superconducting solenoids was below 5 mT, and the retuned maximum gradient in normal quadrupoles was up to 9.1 T/m. Consequently, the local compensation schemes allow a sustainable linac operation.

Thus, we propose to operate with a double injector up to the end of the HWR section, with one operating as the main injector and the other as a hot standby, followed by a fully modular SRF linac, local compensations based on *k-out-of-n* redundancy. In case of any beam trips in the linac, the MPS system will stop the beam in 10 μs. If the failure appears in the main injector, the hot standby injector will be switched in. We assume the time to change the polarity of the switch dipole to be about 1.5 s [28] and approximately 3 s more to check the performance. Thus, the resume beam time was predicted to be about < 5 s. For a failure located downstream of the HWR section, reliability is ensured by using local compensations. The detuning process and parameter setting are foreseen to be < 2 s, and the stability test is about 3 s, a total time of 5 s. The time intervals were based on MYRRHA linac [3,28] and expert colleague opinions. In summary, the beam downtime due to failures is expected to be reduced to < 5 s in the entire linac, which is suitable for the most stringent requirement of the JAEA-ADS project.

This work represents the first step in the development of local compensation strategies and a database of Faulty-elements compensations that will be tested and updated during the commissioning of the beam. To this end, several challenges must be addressed to guarantee the viability of these compensations: robust diagnostic systems that trustworthily and quickly detect an abnormal element behavior, efficient detuning systems for the Faulty element, a fast communication system to implement the compensation settings, and a suitable protocol for returning to the baseline configuration once the Faulty element is recovered. Furthermore, as the availability becomes small for a system composed of many elements, we will reoptimize the lattice to reduce the number of SRF cavities by relaxing their parameters. Thus, the availability will be improved, and the costs will be reduced. To this end, extensive R&D and close collaborations with other ADS projects are mandatory for solving these demands.

ACKNOWLEDGMENTS

The author Bruce would like to thank Robert A. Jameson, Hayanori Takei, and the members of the JAEA-ADS for their comments and suggestions. This work was financially supported by the Ministry of Education, Culture, Sports, Science, and Technology (MEXT) as the Subsidy for Research and Development on Nuclear Transmutation Technology through the Japan Atomic Energy Agency (JAEA).

APPENDIX A: MISMATCH

The horizontal mismatch (M_x) factor between two ellipses beam with the same emittance

$$\varepsilon_x(s) = \gamma_{x1}(s)x^2 + 2\alpha_{x1}(s)xx' + \beta_{x1}(s)x'^2, \quad \text{(A1)}$$

and

$$\varepsilon_x(s) = \gamma_{x2}(s)x^2 + 2\alpha_{x2}(s)xx' + \beta_{x2}(s)x'^2, \quad \text{(A2)}$$

is calculated as

$$M_x = \sqrt{\frac{1}{2}(R + \sqrt{R^2 - 4})} - 1, \quad \text{(A3)}$$

where $R = \beta_{x1}(s)\gamma_{x2}(s) + \beta_{x2}(s)\gamma_{x1}(s) - 2\alpha_{x1}(s)\alpha_{x2}(s)$. Similar for the other two projections, $y - y'$ and $z - z'$ [29].

APPENDIX B: SUMMARY TABLES OF THE FAULT TOLERANCE STUDIES

TABLE VI. Summary of the beam optics performance for single SRF cavity failures.

			$\Delta\varepsilon/\varepsilon_0$		Beam mismatch		
Faulty cavity	Location	Number of retuned cavities (before + after)	Transverse (%)	Longitudinal (%)	Transverse	Longitudinal	Maximum retuned cavity power (kW)/(%)
26	SSR1 (beginning)	0 + 4	2.11	19.31	0.02	0.06	4/28
27	SSR1 (beginning)	1 + 3	2.10	22.74	0.01	0.05	4/29
55	SSR1 (middle)	4 + 3	2.92	13.67	0.01	0.04	11/28
56	SSR1 (middle)	3 + 3	3.29	21.65	0.02	0.08	12/26
90	SSR1 (end)	4 + 3	1.02	4.70	0.04	0.02	17/28
91	SSR1 (end)	4 + 4	0.81	2.92	0.02	0.01	16/25
92	SSR2 (beginning)	3 + 4	1.84	14.59	0.03	0.06	15/11
93	SSR2 (beginning)	4 + 3	0.99	2.28	0.00	0.01	17/25
94	SSR2 (beginning)	5 + 2	1.10	1.78	0.00	0.02	18/27
124	SSR2 (middle)	4 + 3	2.78	5.05	0.01	0.03	56/24
125	SSR2 (middle)	3 + 3	0.20	0.51	0.01	0.02	69/22
126	SSR2 (middle)	4 + 3	−0.74	1.14	0.01	0.01	70/20
161	SSR2 (end)	3 + 4	0.18	1.14	0.01	0.01	77/18
162	SSR2 (end)	3 + 4	0.43	6.08	0.02	0.03	40/21
163	SSR2 (end)	4 + 3	0.67	7.59	0.02	0.03	40/18
164	EllipR1 (beginning)	4 + 3	0.24	8.23	0.01	0.03	70/20
165	EllipR1 (beginning)	4 + 3	0.60	5.44	0.01	0.02	154/24
166	EllipR1 (beginning)	3 + 4	1.65	6.20	0.01	0.03	117/25
191	EllipR1 (middle)	4 + 3	0.59	−1.01	0.01	0.02	147/17
192	EllipR1 (middle)	3 + 4	1.15	11.77	0.01	0.03	238/18
193	EllipR1 (middle)	4 + 3	−0.07	1.52	0.01	0.03	230/18
221	EllipR1 (end)	4 + 3	0.08	0.38	0.01	0.02	233/19
222	EllipR1 (end)	4 + 3	0.58	0.76	0.02	0.03	252/23
223	EllipR2 (end)	4 + 3	0.00	1.52	0.01	0.03	257/20
224	EllipR2 (beginning)	2 + 3	0.76	1.52	0.03	0.06	255/23
225	EllipR2 (beginning)	2 + 3	0.84	1.14	0.02	0.07	246/22
226	EllipR2 (beginning)	3 + 3	−0.18	1.39	0.01	0.01	233/17
227	EllipR2 (beginning)	3 + 4	−0.16	6.20	0.03	0.03	330/22
228	EllipR2 (beginning)	4 + 3	0.10	1.27	0.01	0.02	330/21
254	EllipR2 (middle)	2 + 3	0.75	−0.51	0.01	0.09	324/22
255	EllipR2 (middle)	3 + 3	0.59	0.00	0.01	0.05	336/22

(Table continued)

TABLE VI. *(Continued)*

Faulty cavity	Location	Number of retuned cavities (before + after)	$\Delta\varepsilon/\varepsilon_0$ Transverse (%)	$\Delta\varepsilon/\varepsilon_0$ Longitudinal (%)	Beam mismatch Transverse	Beam mismatch Longitudinal	Maximum retuned cavity power (kW)/(%)
256	EllipR2 (middle)	3 + 3	0.68	1.02	0.01	0.06	332/22
257	EllipR2 (middle)	3 + 2	1.07	1.52	0.02	0.09	346/22
258	EllipR2 (middle)	3 + 2	0.88	1.02	0.01	0.09	346/22
289	EllipR2 (end)	2 + 3	0.09	0.13	0.01	0.04	347/22
290	EllipR2 (end)	3 + 2	−0.17	0.25	0.03	0.08	347/22
291	EllipR2 (end)	3 + 2	0.04	0.13	0.03	0.09	347/22
292	EllipR2 (end)	4 + 1	0.04	0.25	0.03	0.09	347/22
293	EllipR2 (end)	5 + 0	0.21	0.25	0.03	0.09	347/22

TABLE VII. Summary of the beam optics performance for multiples cavity failures.

Case	Faulty cavities	Number of retuned cavities (before + after)	Number of retuned magnets (before + after)	$\Delta\varepsilon/\varepsilon_0$ Transverse (%)	$\Delta\varepsilon/\varepsilon_0$ Longitudinal (%)	Mismatch Transverse	Mismatch Longitudinal	Maximum retuned Cavity power (kW)/(%)	Maximum retuned Magnetic field (T)/(%)
Multiple SRF cavity independent periods	26, 91, 163, 223 and 293	31[a]	0	8.88	62.91	0.01	0.10	347/22	0/0
FullPer I (First SSR1)	26–27	0 + 4	0	21.38	145.62	0.06	0.22	4/28	0/0
FullPer II (Last SSR1)	90–91	4 + 9	3 + 6	7.39	38.71	0.03	0.13	17/25	1.8/28
FullPer III (Last SSR2)	161–163	6 + 9	0 + 6	6.78	99.11	0.02	0.12	77/17	2.7/25
FullPer IV (Last EllipR1)	221–223	6 + 15	0 + 6	1.97	59.37	0.12	0.07	272/20	0.3/7
FullPer V (Last EllipR2)	289–293	25 + 0	6 + 0	−1.84	9.64	0.04	0.16	346/22	0.3/4

[a]This is the total numbers of retuned SRF cavities. The local compensation configuration for each SRF cavity can be found in Table VI.

TABLE VIII. Summary of the beam optics performance for magnets failures.

Faulty magnet	Location	Number of retuned magnet (before + after)	Number of retuned cavities (before + after)	$\Delta\varepsilon/\varepsilon_0$ Transverse (%)	$\Delta\varepsilon/\varepsilon_0$ Longitudinal (%)	Beam mismatch Transverse	Beam mismatch Longitudinal	Maximum retuned Cavity power (kW)/(%)	Maximum retuned Magnetic field (T)/(%)	Minimum[a] Aperture/Maximum transverse size
26	SSR1 (beginning)	1 + 3	0 + 2	12.37	17.79	0.01	0.07	4/28	3.9/300	1.19
41	SSR1 (middle)	3 + 4	2 + 6	10.56	12.79	0.01	0.01	12/28	3.5/17	1.19
58	SSR1 (end)	3 + 6	2 + 7	−0.19	0.38	0.01	0.01	18/9	2.9/4	1.13
59	SSR2 (beginning)	3 + 3	0 + 3	8.54	6.98	0.03	0.01	15/9	2.3/21	1.13
70	SSR2 (middle)	3 + 3	3 + 8	12.33	15.15	0.02	0.05	70/20	4.8/33	1.16
82	SSR2 (end)	2 + 4	0 + 9	2.31	0.38	0.02	0.01	41/17	0.2/330	1.29
83	Transition SSR2-EllipR1	2 + 2	0 + 9	−0.38	0.76	0.01	0.01	55/16	0.1/1.2	1.35

(Table continued)

TABLE VIII. *(Continued)*

				$\Delta\varepsilon/\varepsilon_0$		Beam mismatch		Maximum retuned		Minimum[a]
Faulty magnet	Location	Number of retuned magnet (before + after)	Number of retuned cavities (before + after)	Transverse (%)	Longitudinal (%)	Transverse	Longitudinal	Cavity power (kW)/(%)	Magnetic field (T)/(%)	Aperture/ Maximum transverse size
85–86	EllipR1 (beginning)	$3+2$	$0+9$	2.06	0.00	0.01	0.01	50/5	0.3/500	1.68
103–104	EllipR1 (middle)	$4+2$	$3+6$	22.35	10.38	0.08	0.05	254/25	0.3/3	1.10
123–124	EllipR1 (end)	$4+0$	$0+0$	5.03	6.46	0.06	0.03	0/0	0.3/25	1.45
125–126	EllipR2 (beginning)	$6+2$	$3+10$	13.23	7.72	0.12	0.12	230/18	0.3/6	1.46
141–142	EllipR2 (middle)	$4+4$	$0+0$	1.51	−2.16	0.05	0.12	0/0	0.4/34	1.35
152–153	EllipR2 (end)	$4+0$	$0+5$	1.78	−1.27	0.02	0.06	335/17	0.3/35	1.74

[a]The minimum ratio between the aperture and the maximum transverse beam size.

[1] K. Tsujimoto, T. Sasa, K. Nishihara, H. Oigawa, and H. Takano, Neutronics design for lead-bismuth cooled accelerator-driven system for transmutation of minor actinide, J. Nucl. Sci. Technol. **41**, 21 (2004).

[2] H. Takei, K. Nishihara, K. Tsujimoto, and H. Oigawa, Estimation of acceptable beam-trip frequencies of accelerators for accelerator-driven systems and comparison with existing performance data, J. Nucl. Sci. Technol. **49**, 384 (2012).

[3] J. L. Biarrotte, Reliability and fault tolerance in the European ADS project, in *Proceedings of CERN Accelerator School on High Power Hadron Machines, CAS-2011, Bilbao, Spain, 2011* (CERN, Geneva, Switzerland, 2013), pp. 481–494.

[4] L. Burgazzi and P. Pierini, Reliability studies of a high-power accelerator for accelerator-driven system applications for nuclear waste transmutation, Reliab. Eng. Syst. Saf. **92**, 449 (2007).

[5] T. Sugawara, H. Takei, and K. Tsujimoto, Investigations of accelerator reliability and decay heat removal for accelerator-driven system, Ann. Nucl. Energy **125**, 242 (2019).

[6] A. Ahmad, B. A. Lindley, and G. T. Parks, Accelerator-induced transients in accelerator driven subcritical reactors, Nucl. Instrum. Methods Phys. Res., Sect. A **696**, 55 (2012).

[7] B. Yee-Rendon, Y. Kondo, F. Maekawa, S. Meigo, and J. Tamura, Design and beam dynamic studies of a 30-MW superconducting linac for an accelerator-driven subcritical system, Phys. Rev. Accel. Beams **24**, 120101 (2021).

[8] J. Galambos, S. Henderson, A. Shishlo, and Y. Zhang, Operational of a superconducting cavity fault recovery at the spallation neutron source, in *Proceedings of the Workshop on Utilisation and Reliability of High Power Proton Accelerators (HPPA5), Mol, Belgium, 2007* (Nuclear Energy Agency of the OECD (NEA), Paris, 2007), pp. 161–170.

[9] J. L. Biarrotte and D. Uriot, Dynamic compensation of an rf cavity failure in a superconducting linac, Phys. Rev. Accel. Beams **11**, 072803 (2008).

[10] F. Bouly, J. L. Biarrotte, and D. Uriot, Fault tolerance and consequences in the MYRRHA superconducting linac, in *Proceedings of the 27th Linear Accelerator Conference (LINAC'14), Geneva, Switzerland, 2014* (JACoW, Geneva, 2014), pp. 297–299.

[11] U. S. Department of Defense, Military Handbook: Electronic Reliability Design Handbook, MILHDBK-338B (Department of Defense of U.S.A, Washington, DC, 1998), pp. 5–31.

[12] A. Saini, R. Prakash, and J. D. Kellenberger, Assessment of operational availability for the PIP-II superconducting radio frequency linear accelerator facility, Nucl. Instrum. Methods Phys. Res., Sect. A **988**, 164874 (2021).

[13] J. L. Biarrotte, M. Novati, P. Pierini, H. Safa, and D. Uriot, Beam dynamics studies for the Fault Tolerance Assessment of the PDS-XADS Linac Design, in *Proceedings of the 9th European Particle Accelerator Conference, EPAC'04, Lucerne, Switzerland, 2004* (JACoW, Geneva, 2004), pp. 1282–1284.

[14] Z. Li, P. Cheng, H. Geng, Z. Guo, Y. He, C. Meng, H. Ouyang, S. Pei, B. Sun, J. Sun, J. Tang, F. Yan, Y. Yang, C. Zhang, and Z. Yang, Physics design of an accelerator for an accelerator-driven subcritical system, Phys. Rev. Accel. Beams **16**, 080101 (2013).

[15] F. Bouly, Method development for cavity failure compensation in a superconducting linac, in *Proceedings of the 12th International Particle Accelerator Conference, IPAC-2021, Campinas, Brazil, 2021* (JACoW, Geneva, 2021), pp. 647–650.

[16] B. Yee-Rendon, J. Tamura, Y. Kondo, K. Nakano, H. Takei, F. Maekawa, and S. Meigo, Fast fault recovery scenarios for the JAEA-ADS Linac, in *Proceedings of PASJ2021, QST-Takasaki Online, Japan, 2021* (PASJ, Takasaki, 2021), pp. 61–65.

[17] F. Bouly, Accelerator driven systems (ADS) & high power linacs, in *Proceedings of the Joint Universities Accelerator School, 2022* (unpublished).

[18] T. P. Wangler, *RF Linear Accelerators* (Wiley-VCH Verlag GmbH & Co. KGaA, New York, 2008).

[19] D. Uriot and N. Pichoff, *TraceWin Manual* (CEA Saclay, Weinheim, 2008), CEA/SACLAY-DRF/Irfu/DACM, 2020, Vol. 2, p. 222.

[20] N. Pichoff and H. Safa, Reliability of superconducting cavities in a high power proton linac, in *Proceedings of the 7th European Particle Accelerator Conference, EPAC 2000, Vienna, Austria, 2000* (JACoW, Geneva, 2001), pp. 2049–2051.

[21] A. Fabich and U. Dorda (private communication).

[22] P. N. Ostroumov, S. H. Kim, E. S. Lessner, K. W. Shepard, and R. E. Laxdal, A new generation of superconducting solenoids for heavy-ion linac application, in *Proceedings of the 21st International LINAC Conference, Gyeongu, Korea, 2002* (Pohang Accelerator Laboratory, Pohang, Korea, 2002), pp. 332–334.

[23] T. Sugawara and K. Nishihara (private communication).

[24] B. Yee-Rendon (unpublished).

[25] B. Sun, J. Tang, F. Yan, Z. Li, C. Meng, and S. Pei, Local compensation-rematch for major element failures in superconducting linacs with very high reliability and low beam loss, Nucl. Instrum. Methods Phys. Res., Sect. A **785**, 77 (2015).

[26] J. M. Lagniel, Excitation of the $\sigma_{\parallel} = 90°$ resonance by the cavity rf accelerating fields, in *Proceedings of the 13th International Particle Accelerator Conference, IPAC-2022, Bangkok, Thailand, 2022* (to be published).

[27] J. P. Carnerio, D. Vandeplassche, L. Medeiros-Romao, R. Salemme, J. L. Biarrotte, F. Bouly, and D. Uriot, Toward a virtual accelerator control system for the MYRRHA linac, in *Proceedings of the 5th International Particle Accelerator Conference, IPAC-2014, Dresden, Germany, 2014* (JACoW, Geneva, 2004), pp. 3122–3124.

[28] E. Froidefond, F. Bouly, P. O. Dumont, and D. Vandeplassche, Study and design of a fast switching magnet for the MYRRHA project, in *Proceedings of the 12th International Particle Accelerator Conference, IPAC-2021, Campinas, Brazil, 2021* (JACoW, Geneva, 2021), pp. 2356–2359.

[29] K. R. Crandall and D. P. Rusthoi, TRACE 3-D documentation, Los Alamos National Laboratory, New Mexico, Report No. UR-97-886, 1990.